Monthly Notices
of the
ROYAL ASTRONOMICAL SOCIETY

MNRAS **430,** 1976–1987 (2013) doi:10.1093/mnras/stt020

MHD instabilities in accretion mounds – I. 2D axisymmetric simulations

Dipanjan Mukherjee,[1]★ Dipankar Bhattacharya[1] and Andrea Mignone[2]

[1]*Inter-University Centre for Astronomy and Astrophysics, Post Bag 4, Pune 411007, India*
[2]*Dipartimento di Fisica Generale, Università degli Studi di Torino, Via Pietro Giuria 1, I-10125 Torino, Italy*

Accepted 2013 January 3. Received 2013 January 3; in original form 2012 June 29

ABSTRACT

We have performed stability analysis of axisymmetric accretion mounds on neutron stars in high-mass X-ray binaries by 2D magnetohydrodynamic (MHD) simulations with the PLUTO MHD code. We find that the mounds are stable with respect to interchange instabilities, but the addition of excess mass destabilizes the equilibria. Our simulations confirm that accretion mounds are unstable with respect to MHD instabilities beyond a threshold mass. We investigate both filled and hollow mounds and for the latter also compute the expected profile of cyclotron resonance scattering features (CRSF). In comparison to the CRSF from filled mounds reported in our earlier work, hollow mounds display wider and more complex line profiles.

Key words: line: formation – MHD – radiation mechanisms: non-thermal – binaries: general – stars: neutron – X-rays: binaries.

1 INTRODUCTION

Neutron stars in accreting X-ray pulsars accrete matter from the companion star either from stellar winds (Davidson & Ostriker 1973) or through disc accretion by Roche lobe overflow (Ghosh, Pethick & Lamb 1977; Koldoba et al. 2002; Romanova et al. 2003). They can be broadly classified into two classes: (1) high-mass X-ray binaries (HMXB) with companion stars of masses several times the solar mass and neutron stars with high surface magnetic field $\sim 10^{12}$ G and (2) low-mass X-ray binaries (LMXB) with companion stars of masses less than a solar mass and neutron star magnetic fields several orders lower in magnitude $\sim 10^{7}$–10^{9} G (see Bhattacharya & van den Heuvel 1991 for a review). In this paper, we consider the effect of accretion on the evolution of surface magnetic field of HMXB sources by the formation of accretion mounds.

The accreted matter in HMXB passes through a shock, gradually settling down on the polar cap to form an accretion mound. X-ray emission from such mounds show characteristic cyclotron resonance scattering features (CRSF; Harding & Preece 1987; Araya & Harding 1999; Araya-Góchez & Harding 2000; Becker & Wolff 2007). The CRSF depends on the magnetic field of the local emitting region, and hence serve as a tool to understand the structure of accretion columns. CRSF often show complex line features and characteristic variations with rotation phase and the luminosity of the neutron star (Coburn et al. 2002; Heindl et al. 2004; Mihara et al. 2007; Lutovinov & Tsygankov 2008). Explaining such features require appropriate modelling of the structure of the accretion column and the effect of accretion induced field distortion from the accretion mound.

Also, several authors propose that diamagnetic screening of the magnetic field can lower the apparent dipole moment of the neutron star (Romani 1990; Cumming, Zweibel & Bildsten 2001; Melatos & Phinney 2001; Choudhuri & Konar 2002; Konar & Choudhuri 2004). Some recent works on magnetic screening by accretion mounds (Payne & Melatos 2004, 2007; Vigelius & Melatos 2008, 2009) report that large mounds of mass $\sim 10^{-5}\,M_{\odot}$ may form on the neutron star, which can then bury the field as the matter spreads on the surface. However, several questions regarding the effects of magnetohydrodynamic (MHD) instabilities (Cumming et al. 2001; Litwin, Brown & Rosner 2001) remain to be addressed fully. Magnetostatic solutions of accretion mounds have earlier been found by several authors including Hameury et al. (1983), Brown & Bildsten (1998), Payne & Melatos (2004) and Mukherjee & Bhattacharya (2012). It was shown in Mukherjee & Bhattacharya (2012, hereafter MB12) that magnetostatic solutions cannot be found for mounds beyond a threshold height (and mass), which may be indicative of the presence of MHD instabilities. Similar results were also reported in Payne & Melatos (2004, hereafter PM04) where closed magnetic loops were seen to form beyond a threshold mound mass.

In this paper, we attempt to study the stability of the accretion mound by 2D axisymmetric MHD simulations with the PLUTO MHD code (Mignone et al. 2007). The study of the full set of MHD instabilities in such mounds requires global 3D simulations. However, results from 2D simulations would help to identify modes that grow despite of the restrictive assumption of axisymmetry. This will be a stepping stone to future 3D simulations where many other modes may grow simultaneously. Here, we investigate the presence of interchange instabilities as predicted for such mounds by Litwin et al. (2001), and also the physical cause of the threshold in mound mass obtained in MB12. To study the latter, we add a small amount of mass to an existing Grad–Shafranov solution and dynamically evolve the system to see if it settles to a new equilibrium state.

★ E-mail: dipanjan@iucaa.ernet.in

This is carried out for different mound sizes up to the threshold mass, at which one expects MHD instabilities to be triggered if the threshold happens to be due to a physical effect.

Our approach differs from that of PM04 in various aspects. We consider a cylindrical geometry with strict containment of the accreted matter in the polar cap, while PM04 consider spherical geometry with mass loading on all field lines up to the equator. Also, we consider degenerate non-relativistic *Fermi* plasma near the polar cap surface instead of the isothermal equation of state used by PM04. As we consider densities as high as $\sim 10^8$ g cm^{-3} inside the mound, a degenerate non-relativistic plasma is more appropriate (see MB12 for a discussion).

Early models of accretion column formed by disc–magnetosphere interaction proposed hollow ring-like accretion column on neutron star poles (Basko & Sunyaev 1976; Ghosh & Lamb 1978, 1979). Several authors have used hollow ring-like accretion columns to fit the pulse profiles of HMXBs (e.g. Leahy 1991; Shakura et al. 1991; Riffert et al. 1993). Panchenko & Postnov (1994) and Klochkov et al. (2008) discuss effects of emission from two disconnected rings to explain the shape of observed pulse profiles and nature of cyclotron features in the emission from Her X-1. Following the formalism of pulse profile decomposition developed by Kraus et al. (1995), ring-like columns have been inferred for sources like Her X-1 (Kraus 2001), 4U 1909+07 (Fürst et al. 2011), A0535+262 (Caballero et al. 2011) and V 0332+53 (Ferrigno et al. 2011). Even for LMXB sources, ring-like polar cap models are preferred for fitting pulse profiles (Poutanen, Ibragimov & Annala 2009; Kajava et al. 2011). We therefore perform a study of the structure and stability of hollow accretion mounds to compare with results from filled mounds. We also perform simulations of CRSF emission from hollow mounds, following the method described in MB12.

We structure the paper as follows: in Section 2, we outline the numerical setup involved in the problem. We discuss the solution of the Grad–Shafranov equation to determine the structure of the static mound. We also discuss details of the setup of the MHD simulations with PLUTO. In Section 3, we discuss the testing of the equilibrium solution with PLUTO. In Section 4, we discuss the method and results of the perturbation analysis with PLUTO to investigate the stability of the mounds. In Section 5, we discuss the results of the simulations of hollow mounds and we summarize the results in Section 6.

2 NUMERICAL SETUP

To test the hydromagnetic stability of the confined mound, we first evaluate the equilibrium solution to the magnetohydrostatic equations by solving the Grad–Shafranov (hereafter GS) equation. The solution of the GS equation is used as initial condition in PLUTO, where perturbation analysis is performed. In the following section, we outline the solution of the GS equation and the setup of the simulation using PLUTO.

2.1 Equilibrium solution from the Grad–Shafranov equation

For an axisymmetric system, one may write the magnetic field in terms of the flux function in cylindrical coordinates as

$$\boldsymbol{B} = \frac{\nabla\psi \times \hat{\boldsymbol{\theta}}}{r} \quad (\boldsymbol{B}_\theta = 0) \tag{1}$$

Using equation (1) in the static Euler equation and using separation of variables in cylindrical coordinates using method of characteristics (as in MB12), we get the GS equation for an adiabatic gas ($p = k_{\rm ad}\rho^\gamma$)

$$\frac{\Delta^2\psi}{4\pi r^2} = -\rho g \frac{{\rm d}Z_0}{{\rm d}\psi}, \tag{2}$$

where g is acceleration due to gravity and density is given by the equation

$$\rho = \left(\frac{g(\gamma-1)}{\gamma {\rm k}_{\rm ad}}\right)^{\frac{1}{\gamma-1}} [Z_0(\psi) - z]^{\frac{1}{\gamma-1}}. \tag{3}$$

$Z_0(\psi)$ is the mound height function which determines the shape of the mound. For our work, we use the equation of state for a degenerate non-relativistic zero temperature *Fermi* plasma with $\mu_e = 2$:

$$\left.\begin{aligned} p &= \left[(3\pi^2)^{2/3}\tfrac{\hbar^2}{5m_e}\right]\left(\tfrac{\rho}{\mu_e m_{\rm p}}\right)^{5/3} \\ &= 3.122\times 10^{22}\left(\tfrac{\rho}{10^6\ {\rm g\ cm^{-3}}}\right)^{5/3}\ {\rm dynes\ cm^{-2}} \end{aligned}\right\} \tag{4}$$

Most of the mound will be dominated by degeneracy pressure except for a thin layer at the top ($\sim$4 cm at 1keV plasma, see MB12 for a discussion). Thus effects of thermal stratification would play a limited role, and the zero temperature degenerate equation of state would be an adequate assumption. We solve the GS equation for an accretion mound of radius $R_{\rm p} = 1$ km, on the poles of a slowly spinning neutron star of mass 1.4 M$_\odot$ and radius $R = 10$ km. The intrinsic field is assumed to be dipolar, which in the polar cap region can be approximated as a uniform field along $\hat{\boldsymbol{z}}$ ($\boldsymbol{B}_{\rm p} = B_0\hat{\boldsymbol{z}}$). We consider Newtonian gravity with constant acceleration:

$$\boldsymbol{g} = -1.86\times 10^{14}\left(\frac{M_*}{1.4\,{\rm M}_\odot}\right)\left(\frac{R_s}{10\,{\rm km}}\right)^{-2}\ {\rm cm\ s^{-2}}\ \hat{\boldsymbol{z}} \tag{5}$$

Our setup is similar to that in Hameury et al. (1983) and Litwin et al. (2001). Following MB12, we carry out most of our analysis for the mound height profile:

$$Z_0(\psi) = Z_{\rm c}\left(1 - \left(\frac{\psi}{\psi_{\rm p}}\right)^2\right), \tag{6}$$

where $Z_{\rm c}$ is the central height of the mound and $\psi_{\rm p} = (1/2)B_0R_{\rm p}^2$. This is a smoothly varying parabolic profile in ψ which describes a filled axisymmetric mound. We also discuss the GS solution for a hollow mound in Section 5, which is specified by the mound height function:

$$Z_0(\psi) = \frac{Z_{\rm c}}{0.25}\left(0.25 - \left(\frac{\psi}{\psi_{\rm p}} - 0.5\right)^2\right) \tag{7}$$

The GS is a coupled non-linear elliptic partial differential equation. We have solved the GS equation by an iterative under-relaxation algorithm with an inner successive over-relaxation loop with Chebyshev acceleration (Press et al. 1993) as is outlined in MB12. For a given polar magnetic field ($B_{\rm p}$), the solutions to the GS equations are obtained up to a threshold height $Z_{\rm max}$, beyond which the numerical scheme does not converge to give an unique solution. Details of the numerical algorithm and convergence of the GS solutions have already been discussed in MB12.

2.2 PLUTO SETUP: INITIALIZATION

We use the Godunov scheme based MHD code PLUTO (Mignone et al. 2007) to test the stability of the confined mound. The solutions of the GS equation are used as initial condition in PLUTO.

The GS solutions are imported into PLUTO using bi-linear interpolation. We use the MHD module of PLUTO to solve the full set of ideal magnetohydrodynamic equations

$$\frac{\partial \rho}{\partial t} + \boldsymbol{v} \cdot \nabla \rho + \rho \nabla \cdot \boldsymbol{v} = \boldsymbol{0} \tag{8}$$

$$\frac{\partial \boldsymbol{v}}{\partial t} + \boldsymbol{v} \cdot \nabla \boldsymbol{v} + \frac{1}{\rho} \boldsymbol{B} \times (\nabla \times \boldsymbol{B}) + \frac{1}{\rho} \nabla p = \boldsymbol{g} \tag{9}$$

$$\frac{\partial \boldsymbol{B}}{\partial t} + \nabla \times (\boldsymbol{v} \times \boldsymbol{B}) = \boldsymbol{0} \tag{10}$$

$$\frac{\partial p}{\partial t} + \boldsymbol{v} \cdot \nabla p + \rho c_s^2 \nabla \cdot \boldsymbol{v} = \boldsymbol{0}, \tag{11}$$

where the factor $1/\sqrt{4\pi}$ is absorbed in the definition of magnetic field and c_s^2 is the speed of sound (which for adiabatic gas is $c_s^2 = \gamma p/\rho$). The system is closed by an equation of state (hereafter EOS) which we choose to be either adiabatic ($\rho\epsilon = p/(\gamma - 1)$) or barotropic for which $p = p(\rho)$. In the second case equation (11) is redundant. To investigate the effects of pressure-driven interchange modes and gravity-driven modes, we perform perturbation analysis with the adiabatic EOS (see Sections 4.1 and 4.2). PLUTO initialization and boundary conditions are provided in terms of primitive variables (ρ, $\boldsymbol{v}$, p, $\boldsymbol{B}$) defined in equation (8)–equation (11). The computation is carried out in conservative variables (ρ, $\rho\boldsymbol{v}$, E, $\boldsymbol{B}$), where $E = \rho\epsilon + \rho\boldsymbol{v}^2/2 + \boldsymbol{B}^2/2$ is the total energy density.

We use the extended generalized Lagrangian multiplier (EGLM) scheme (Mignone & Tzeferacos 2010; Mignone, Tzeferacos & Bodo 2010) to preserve the $\nabla \cdot \boldsymbol{B} = \boldsymbol{0}$ constraint. The EGLM scheme preserves the divergence criterion by modifying the induction equation (equation 10) with a scalar field function $\psi_{\rm GLM}$ (Dedner et al. 2002) and also the energy momentum equations with extra source terms. This scheme transports the non-zero divergence errors to the boundary of the domain at the fastest possible characteristic speed, and damp them at the same time.

For our problem, we have found that the HLL Riemann solver (Toro 2008), HLLD Riemann solver (Miyoshi & Kusano 2005) and TVD Lax–Friedrichs solver (Toro 2008) combined with EGLM scheme provide solutions free from numerical instabilities. Due to the presence of very sharp gradients in the physical quantities, higher order schemes need to be employed to reduce numerical errors. A third-order Runge–Kutta scheme is used for time evolution and a third-order accurate piece-wise parabolic interpolation scheme (PPM scheme as in Colella & Woodward 1984) has been employed.

The simulations were set up using square cells ($\Delta r \simeq \Delta z$) to minimize numerical errors. The resolutions used were less than $\sim$0.5 m as listed in Table 1 for some sample runs. The physical variables in PLUTO are scaled to non-dimensional forms before initialization. For example for mounds with polar magnetic field $B_{\rm p} = 10^{12}$ G, we use $\rho = 10^6\,{\rm g\,cm^{-3}}$ as the density unit, $L_0 = 10^5$ cm as the length unit, $B_0 = 10^{12}$ G as the magnetic field unit and $V_{A0} = B_0/\sqrt{4\pi\rho} = 2.82 \times 10^8\,{\rm cm\,s^{-1}}$ as the velocity unit. In these units, time is measured in units of $t_{\rm A} = L_0/V_{\rm A0} = 3.55 \times 10^{-4}$ s, which can be taken as the mean Alfvén time, while the scale velocity is the mean Alfvén velocity. A unique Alfvén velocity cannot be prescribed for the whole domain as the Alfvén speeds will vary over the domain depending on local density and magnetic field.

Table 1. Sample resolutions for simulation runs.

$Z_{\rm c}$	$B_{\rm p}$	$N_r \times N_z$	Δl ($\Delta z \simeq \Delta r$)
72 m	10^{12} G	1024 × 144	∼0.43 m
65 m	10^{12} G	1088 × 104	∼0.46 m
55 m	10^{12} G	1272 × 88	∼0.39 m
50 m	10^{12} G	1024 × 80	∼0.43 m
25 m	10^{11} G	1920 × 72	∼0.2 m

2.3 Boundary conditions

For stability studies, we run the simulations with either fixed boundaries where quantities are kept fixed to initial values ($Q = Q_0$) or fixed gradients where the initial gradients are preserved. The fixed gradient boundary implies outflow of perturbed quantities as gradients of perturbations are set to zero ($\nabla Q = \nabla Q_0 + \nabla \tilde{Q} \rightarrow \nabla Q_0$, $\nabla \tilde{Q} = \boldsymbol{0}$). The standard outflow boundary condition ($\nabla Q = 0$) is inapplicable for our problem as the initial solution has non-zero gradients at the boundaries of the domain. The fixed gradient boundary condition is applied to the upper and the rightmost boundary. For filled mounds, the inner-left boundary is kept fixed as it is close to or equal to the axis of the column. For hollow mounds, the inner-left boundary is kept at a fixed gradient to allow for inward flow of perturbed matter. The bottom boundary is kept fixed to simulate a hard crust. The setup with fixed gradients on the outer sides and fixed crust gives numerically stable solutions, as tested from the simulations of the equilibrium solutions obtained from the GS solver (see Section 3).

3 EQUILIBRIUM STUDIES

The GS solutions for adiabatic mounds have density profiles which go to zero beyond $Z_0(\psi)$ (see equation 3). To avoid unrealistic Alfvén velocities, we restrict the computation domain inside the mound such that Alfvén speeds in the mound are non-relativistic. A typical computation domain is depicted in Fig. 1 for a mound of height $Z_{\rm c} = 65$ m. We first evolve the initial equilibrium solution without applying perturbation in order to check the stability of the

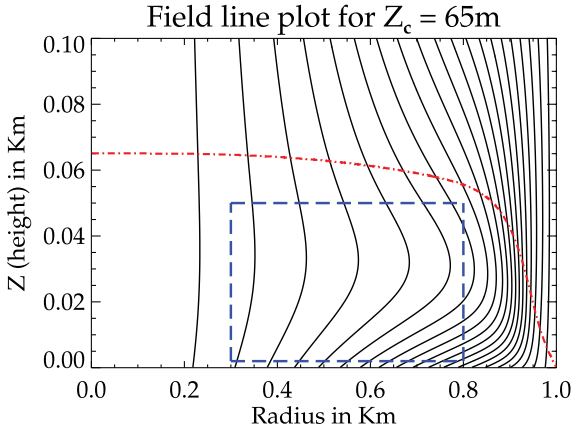

Figure 1. Field lines for a mound of height $Z_{\rm c} = 65$ m with polar unloaded field $B_{\rm p} = 10^{12}$ G. The dash–dotted line in red denotes the top of the mound beyond which density is zero. The total mass of the mound is $\sim 1.63 \times 10^{-12}\,{\rm M}_\odot$. The dashed blue box in the middle is the PLUTO computation domain, chosen to keep Alfvén velocities non-relativistic. The range of density is $\sim 2.1 \times 10^6 - 6.7 \times 10^6$ g cm^{-2} at the top of the mound and $\sim 3.02 \times 10^7 - 5.7 \times 10^7$ g cm^{-2} at the bottom.

numerical schemes and also to study the effects of initial transients contributed by the numerical errors accumulated in interpolating the solution from GS grid to PLUTO domain.

The solutions have been evolved to $t \sim 80t_A$ for different choices of schemes. For the set of schemes outlined in Sections 2.2 and 2.3, the equilibrium solution remains intact with very small buildup of internal flow velocities. For example, for a mound of height $Z_c = 72$ m, at $t \sim 80t_A$, the maximum velocity is $\sim 7.5 \times 10^{-4}$ in normalized units ($\sim 2.15 \times 10^5$ cm s^{-1}, which is much smaller than typical scale velocities). This shows that the schemes used are free from artificial numerical effects and also verifies the validity of the equilibrium solution obtained from the GS solver.

4 PERTURBATION ANALYSIS

We perturb the equilibrium solution by adding a normalized perturbation field $\xi(r, z)$ to any of the physical quantities

$$Q = Q_0(1 + \eta\xi(r, z)), \tag{12}$$

where η is a positive number signifying the perturbation strength. The perturbations are kept away from the boundaries on all sides. This is to preserve the equilibrium at the boundary layers and avoid spurious interaction with the boundary. For our studies, we apply a random perturbation on the density inside the simulation domain, namely ξ is assigned a random value at each grid point within the perturbation zone. The edges of the perturbing region are smoothed with an exponential function to avoid sharp gradients which can lead to spurious effects. The lack of any preferred perturbation scale should allow the growth of the fastest growing modes. The perturbation analysis is performed for mounds of different heights up to the threshold height Z_{max} beyond which the GS solver does not converge, as has been found in MB12.

4.1 Zero-mean perturbations: interchange modes

Zero-mean random perturbation with $\langle\xi\rangle = 0$, implies rearranging of density from the equilibrium solution without adding any net mass. In this case, the system quickly converges to stable pockets of perturbations, irrespective of perturbation strength (η in equation 12). See Fig. 2 for the results of a run with perturbation strength $\eta =$ 10 per cent. The system settles down to an energy state close to the original equilibrium value (see Fig. 3). However, for larger perturbation strengths, a longer time is taken to relax into stable pockets of perturbed matter. For example, a mound with $B_p = 10^{12}$ G and $Z_c = 65$ m stabilizes after $t \sim 1t_A$ for $\eta = 2$ per cent and $t \sim 4t_A$ for $\eta = 10$ per cent.

The perturbation tests have been carried out for mounds of different heights and polar magnetic field strengths. No instabilities are seen at the threshold mound heights, e.g. $Z_c \sim 72$ m for $B = 10^{12}$ G and $Z_c \sim 25$ m for $B = 10^{11}$ G etc. The simulations show that the mounds are stable with respect to small departures from equilibrium resulting from rearrangement of flux tubes. Thus interchange or ballooning modes are not seen in 2D axisymmetric simulations of the mounds.

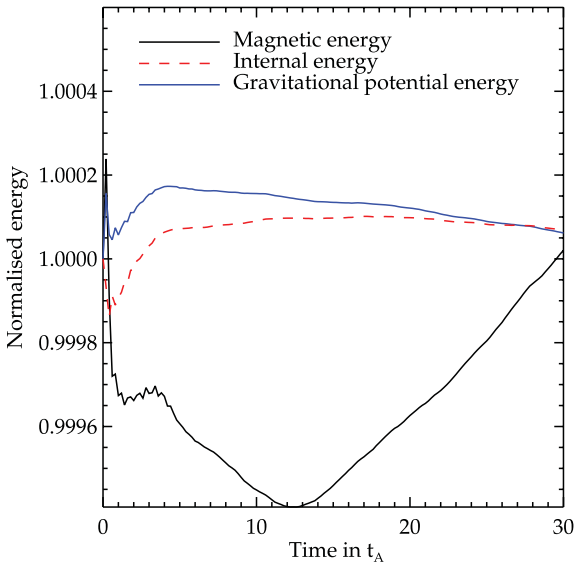

Figure 3. Energy components for zero-mean random perturbation run, normalized to their initial value. Magnetic energy is normalized to 3.7×10^{22}, internal energy to 8.9×10^{23} erg and gravitational potential energy to 6.7×10^{23} erg. The internal and gravitational energy components remain almost constant ($\sim$0.02 per cent change from initial value). The magnetic energy initially decreases as the pockets of perturbed matter settle down, eventually returning to its initial value. This indicates that the system is stable, and when perturbed, settles to an energy state close to the original equilibrium value.

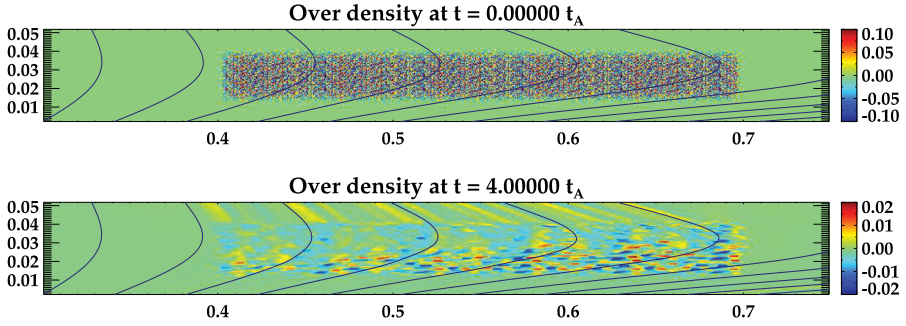

Figure 2. Overdensity: $(\rho - \rho_{eq})/\rho_{eq}$ for zero-mean perturbation runs for a mound of height $Z_c = 65$ m, polar magnetic field $B_p = 10^{12}$ G and perturbation strength $\eta = 10$ per cent. ρ_{eq} is the unperturbed density from the equilibrium solution. The vertical axis is the height above neutron star surface in kilometres. The horizontal axis is the radius (cylindrical geometry) in kilometres. The PLUTO simulation was carried out with a grid of size 1024×120. Random perturbation is provided within a rectangular box inside the domain, away from the boundaries. The edges of the perturbation region are smoothed exponentially. The perturbation slowly weakens and relaxes into stable pockets of perturbed density by $t \sim 4t_A$ (bottom panel). The magnetic field lines are plotted in black.

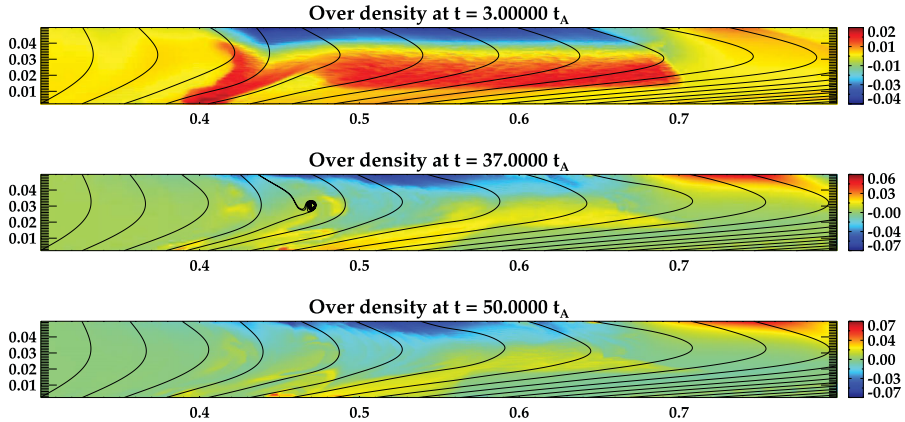

Figure 4. Overdensity: $(\rho - \rho_{\rm eq})/\rho_{\rm eq}$ at different times for a positive density perturbation with strength $\eta = 3$ per cent in a mound of height $Z_{\rm c} = 65$ m and polar magnetic field $B_{\rm p} \sim 10^{12}$ G. The simulation was carried out with a grid of size 1088×104. The horizontal and vertical axes are the same as in Fig. 2. The perturbations result in the formation of closed loops but the solution eventually settles down to a steady state.

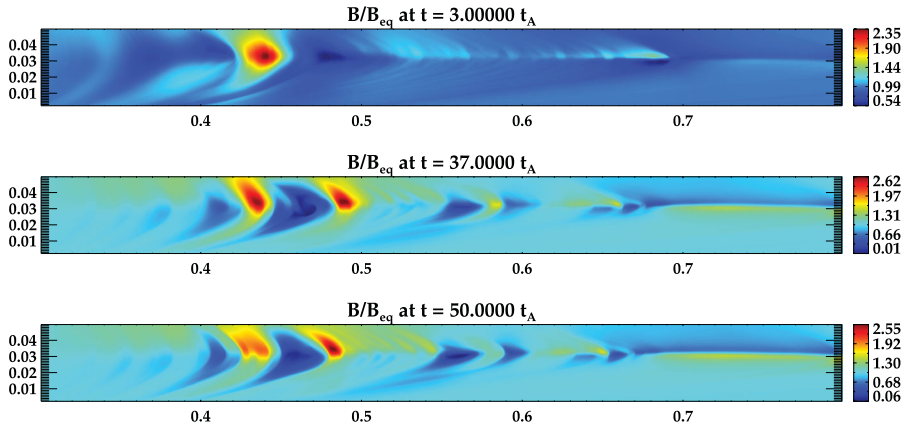

Figure 5. Magnetic field magnitude normalized to the local equilibrium value for the simulation described in Fig. 4. Bunching of field lines forms pockets of excess field over equilibrium value, which eventually get smeared and start to dissipate.

4.2 Adding excess mass to equilibrium solution

In order to study the effect on the mound of the addition of matter which eventually descends due to gravity, we apply a positive definite random perturbation field: $\langle \xi \rangle > 0$ on the density without any corresponding change in pressure. Such a change in density implies local departure of $k_{\rm ad}$ from that in equation (4). In this work, we do not attempt to model the exact composition of the accretion mound. The perturbations were set up to ensure that the added matter is heavier than its surroundings and will descend due to gravity, thus triggering the gravity-driven modes. However, a change in $k_{\rm ad}$ can indeed occur due to changes in chemical composition, e.g. $\eta \sim 5$ per cent local perturbation on a $Z_{\rm c} \sim 65$ m mound would correspond to a change of mean molecular weight by $\Delta\mu_e \sim 0.1$.

The added mass settles down along the field lines, dragging and distorting the equilibrium field configuration in the process. For small perturbation strengths ($\eta \simeq 1$ per cent for mound of height $Z_{\rm c} = 65$ m) the matter quickly settles down to a new equilibrium, without appreciable distortion of the field lines. With an increase in η beyond a threshold, e.g. $\eta_{\rm T} \sim 3$ per cent for $Z_{\rm c} = 65$ m and $B_{\rm p} = 10^{12}$ G mound, magnetic Rayleigh–Taylor type instabilities are triggered by descending heavier matter and results in the formation of closed loops due to the reconnection of field lines (see Fig. 4).[1] Bunching of field takes place in the radial direction (e.g. Fig. 5) and the system eventually relaxes to a steady state.

Furthermore, increase in perturbation strength, e.g. $\eta \sim 5$ per cent for $Z_{\rm c} = 65$ m, disrupts the equilibria completely. Several closed loops are formed across the perturbed region (see Figs 6 and 7). Individual closed loops merge to form larger knots without showing any signs of decay. From Fig. 8 we see that the gravitational potential energy and internal energy decreases from initial value, whereas magnetic energy increases with time. This indicates that internal flows stretch and twist the field lines converting internal energy and gravitational energy to magnetic energy. The system does not relax to a steady state within the run time of the simulation ($t \sim 50 t_{\rm A}$). Thus, for a mound with $Z_{\rm c} = 65$ m and $B_{\rm p} = 10^{12}$ G the threshold perturbation strength is $\eta_{\rm T} \sim 3$ per cent beyond which gravity- and pressure-driven modes disrupt the MHD equilibria.

Convergence has been tested by running the simulations for successive higher resolutions, e.g. for $Z_{\rm c} = 65$ m, $B_{\rm p} = 10^{12}$ G with

[1] Note that although the simulation is ideal MHD, numerical resistivity allows dissipation and reconnection to occur.

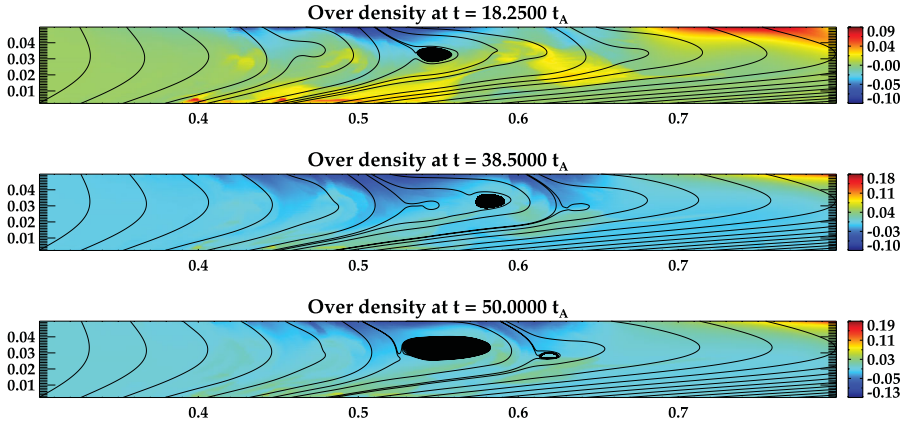

Figure 6. Overdensity $(\rho - \rho_{\rm eq})/\rho_{\rm eq}$ at different times for a positive density perturbation with strength $\eta = 5$ per cent in a mound of height $Z_{\rm c} = 65$ m and $B_{\rm p} = 10^{12}$ G. The simulation was carried out with a grid of size 1088×104. The horizontal and vertical axes are the same as in Fig. 2. The reconnection of field lines forms closed loops at multiple sites. The system does not relax to any steady state solution within the duration of the run. The closed loops grow with time indicating the onset of unstable modes.

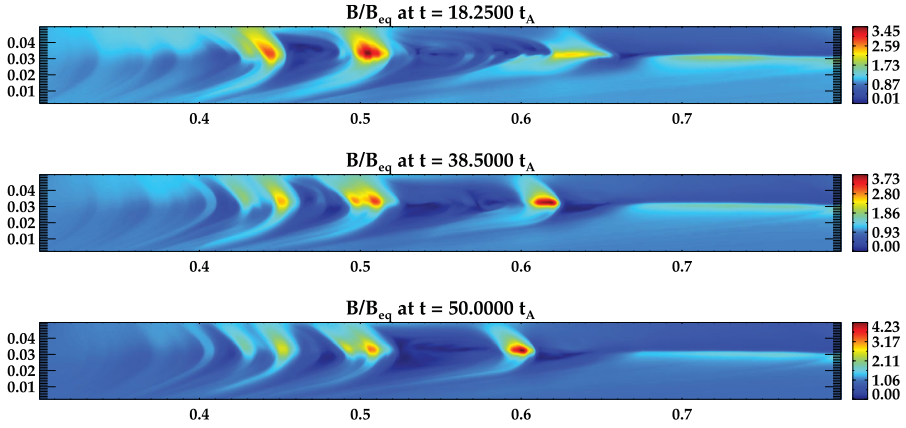

Figure 7. Magnetic field magnitude normalized to the local equilibrium value for the simulation described in Fig. 6. The bunching of field lines cause pockets of excess field over equilibrium value which do not settle to any steady state.

positive random perturbation of strength $\eta = 5$ per cent, simulations were carried out for resolutions 1088×104, 2176×208 and 4352×416. It was seen that MHD instabilities persist on increase of resolution. Increase in resolution reduces numerical resistivity, thus decreasing cross-field diffusion. The field lines are then more prone to be deformed by gravity-driven modes triggered by the weight of the overlying matter.

With an increase in mound height, it is easier to excite such unstable behaviour. The threshold perturbation strength is larger for mounds of smaller height: for $Z_{\rm c} = 45$ m and $B_{\rm p} = 10^{12}$ G, $\eta_{\rm T} \sim 7$ per cent. Mounds near the GS threshold height $Z_{\rm max}$ ($\sim$72 m for $B_{\rm p} = 10^{12}$ G; $\sim$25 m for $B_{\rm p} = 10^{11}$ G) are only marginally stable at $\eta_{\rm T} \simeq 1$ per cent. Thus, mounds higher than a threshold (as previously obtained in MB12) are prone to gravity-driven Rayleigh–Taylor and pressure-driven instabilities on the addition of excess mass, and stable magnetostatic solutions cannot be obtained.

5 HOLLOW MOUND

5.1 Grad–Shafranov for hollow mounds

For systems with magnetospheric accretion, mass loading at the accretion disc takes place over a finite range of accretion disc radii ($\Delta_r \sim 0.03 R_{\rm A}$, $R_{\rm A} \equiv$ Alfvén radius; e.g. Ghosh & Lamb 1978, 1979). The inner edge of the polar cap ring[2] for such systems will be

$$R_{\rm pi} = R_{\rm p}\left(1 - \frac{\Delta_r}{2R_A}\right) \tag{13}$$

while the outer edge of the polar cap radius is $(R_{\rm s}/R_{\rm A})^{1/2} R_{\rm s}$ (Poutanen et al. 2009), $R_{\rm s}$ being the neutron star radius. For small values of Δ_r the columns would be hollow and thin walled. On the surface of the star this would create an accretion ring around the polar cap instead of a filled mound. To model such an accretion ring, we choose the mound height function to give a hollow mound in which the density falls off to zero both at the axis and at the polar cap radius.

For the solution presented in Fig. 9, we use a mound height profile as in equation (7) with $Z_{\rm c} = 45$ m and $B_{\rm p} = 10^{12}$ G. The solution shows considerable distortion of field lines on both sides of the apex ($r \sim 698$ m). This is in contrast to the case of filled mounds, where curvature of field lines occur towards the outer edge. Larger curvature of field lines allow larger mass to be accumulated per flux tube, as compared to that of filled mounds. Hence, although the

[2] which corresponds to the outermost radius in the accretion disc $\sim R_{\rm A} + \Delta_r$, where mass loading begins.

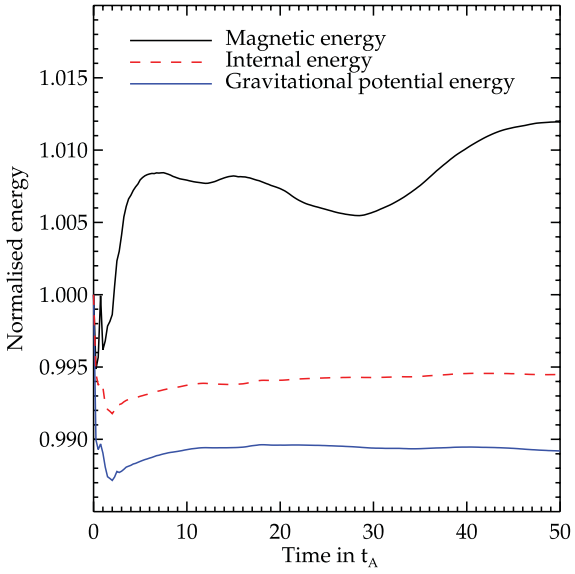

Figure 8. Energy components for random positive perturbation run ($\eta =$ 5 per cent), normalized to their initial value. Magnetic energy is normalized to 5.2×10^{22} erg, internal energy to 9.9×10^{23} erg and gravitational potential energy to 7.5×10^{23} erg. The initial energy is dominated by internal and gravitational energy. The gravitational and internal energy decrease as the system moves to a lower energy state following the perturbation. The magnetic energy is seen to increase due to stretching of field lines due to internal flows.

central part is hollow the total mass contained in the hollow mound ($M \sim 5.87 \times 10^{-13}\,\mathrm{M}_\odot$) is comparable to that of a filled mound of the same height and field ($M \sim 5.09 \times 10^{-13}\,\mathrm{M}_\odot$ for $Z_\mathrm{c} \sim 45$ m and $B_\mathrm{p} \sim 10^{12}$ G and a parabolic profile as in equation 6).

The family of GS solutions for hollow mounds behave similarly as for filled mounds. With the increase in maximum mound height Z_c, the GS solutions show larger curvature of field lines on both sides of ridge apex. The GS solutions fail to converge for mounds greater than a threshold height for a given magnetic field. For the mound height profile of equation (7), the threshold height is around $Z_\mathrm{max} \sim 47$ m for a polar magnetic field $B_\mathrm{p} = 10^{12}$ G.

5.2 Stability analysis of hollow mounds

Using the GS solutions for hollow mound, we perform stability analysis with PLUTO. The results are similar to that of a filled mound. Zero-mean density perturbations do not show growth of the perturbed region, indicating that the mounds are intrinsically stable with respect to interchange modes. For positive perturbations in density, closed loops are formed after a threshold perturbation strength. See Figs 10 and 11 for the results of a run with $\eta = 5$ per cent. The closed loops form quickly within a few Alfvén times and migrate away from the centre, on both sides of the central height. This results in the formation of alternate regions of enhanced and reduced magnetic field due to the bunching of field lines, which have considerable departure from equilibrium solution. The field knots dissipate gradually as they migrate outwards.

5.3 Cyclotron lines from hollow mounds

Following the algorithm outlined in MB12, we have simulated the CRSF that will be observed in the emitted spectrum from a hollow mound. The spectra have been calculated by integrating the emission from different parts of the mound towards a given line

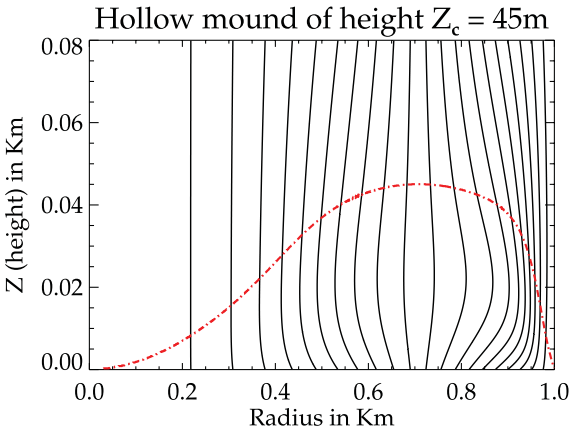

Figure 9. The field lines from GS solution for a hollow mound with mound height function given by equation (7), $Z_\mathrm{c} = 45$ m and $B_\mathrm{p} = 10^{12}$ G. The maximum height Z_c occurs at ∼698 m from the axis. The red dashed line represents the top of the mound.

of sight (hereafter los). We assume a Gaussian absorption profile whose depth and width are evaluated from the interpolated results of Schönherr et al. (2007) for the slab 1–0 geometry. As in MB12, the line centre of the CRSF is obtained from the expression

$$E_n = n E_{\mathrm{c}0}\sqrt{1-u}\left(1 - \frac{n}{2}\left(\frac{E_{\mathrm{c}0}}{511\,\mathrm{keV}}\right)\sin^2\theta_{ab}\right) \qquad (14)$$

where $n = 1, 2, 3\ldots$ is of the order of the harmonic, $E_{\mathrm{c}0} = 11.6 B_{12}$ in keV, θ_{ab} is the angle between the direction of emission and local magnetic field and $u = r_\mathrm{s}/r$, r_s being the Schwarzschild radius. Emission from the inner part of the hollow mound may be blocked by the walls on the opposite side. In Appendix (A), we explain the scheme we follow to account for such shielding.

For the simulated spectra shown in Fig. 12, we consider emission from a single pole at inclination angle $\eta_\mathrm{p} = 10^\circ$ and an los at $i = 60^\circ$, both measured from the spin axis. The spectrum shows multiple absorption features due to the large variation of field strength at the top of the mound (see Fig. 13). The different absorption features correspond to emission from different locations on the top of the mound, with different magnetic field values. The nature of this spectrum is significantly different from that expected from a filled parabolic mound of the same height (see Fig. 12). When convolved with a Gaussian of standard deviation ∼10 per cent of the local energy, to simulate the finite resolution of a detector (see MB12 for details), the spectrum becomes a broad absorption feature.

6 DISCUSSION AND SUMMARY

(i) **Absence of interchange mode instabilities:** in this paper, we have tested for the stability of magnetostatic accretion mounds by MHD simulations using the PLUTO MHD code. From perturbation analysis, we conclude that mounds are stable with respect to interchange or ballooning modes in 2D axisymmetric simulations.[3] Linear stability analysis by Litwin et al. (2001) predict the onset of ballooning modes for a threshold plasma β ($\beta = p/(B^2/8\pi)$). However, such modes are inherently multi-dimensional in nature, with finite toroidal and zero poloidal wave vectors, normal to the

[3] Note that in this paper, we consider a $T = 0^\circ$ K *Fermi* gas. However, finite plasma temperature can induce additional thermal modes (Cumming et al. 2001), which have not been explored here.

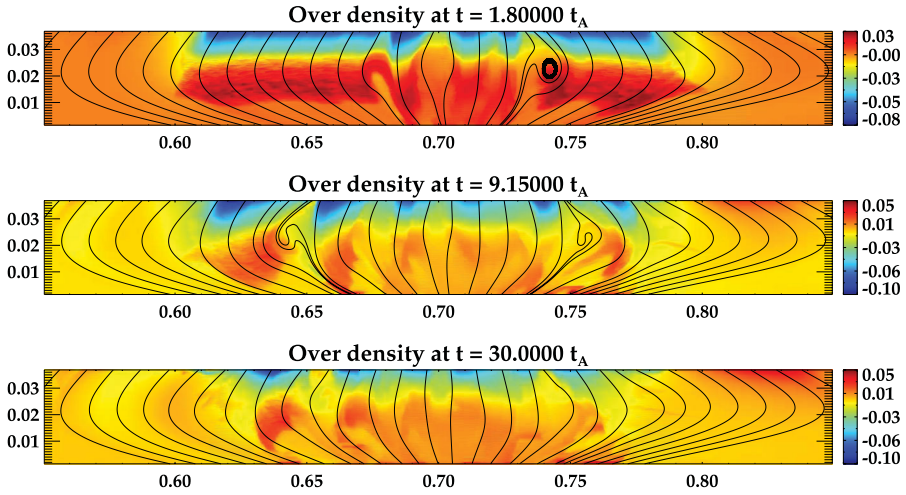

Figure 10. Overdensity $(\rho - \rho_{\rm eq})/\rho_{\rm eq}$ and field line for a hollow mound of maximum height $Z_{\rm c} = 45$ m and polar magnetic field $B_{\rm p} = 10^{12}$ G with a positive density perturbation of strength $\eta = 5$ per cent. The simulation was carried out for a grid of size 1144×136. The vertical and horizontal axes are the same as in Fig. 2. The perturbation results in the formation of closed loops at multiple sites near the centre, very early in the simulation run.

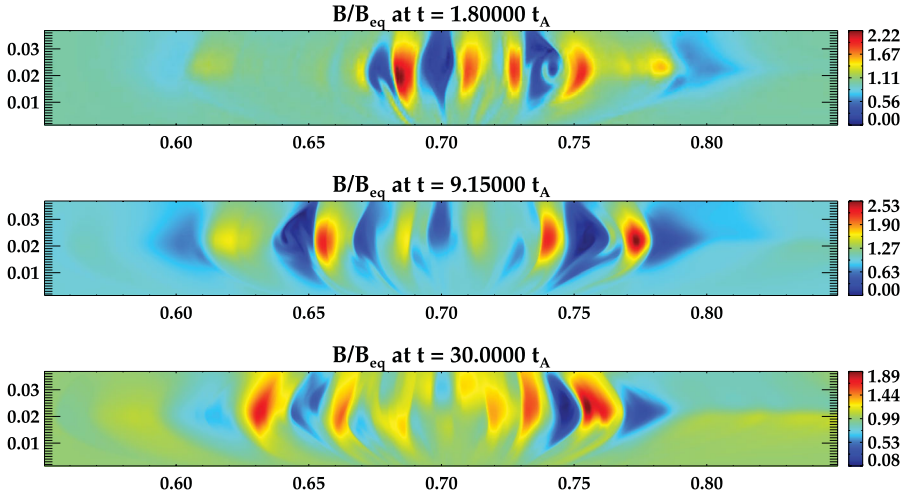

Figure 11. Magnetic field magnitude normalized to the local equilibrium value for the simulation described in Fig. 10. The bunching of field lines in radial direction causes alternate regions of enhanced field strengths. The closed loops and pockets of enhanced fields migrate to the radial boundaries and eventually dissipate.

local magnetic field (see Freidberg 1982, for a review of MHD instabilities in confined plasma). Hence, such modes cannot be excited in an axisymmetric 2D simulation.

Litwin's approximate analytical estimates give a threshold $\beta_{\rm T} \sim 11.7(R_{\rm p}/Z_{\rm c})$ for $\gamma \sim 5/3$, beyond which MHD instabilities will set in. For GS solution of a filled mound with $Z_{\rm c} = 45$ m and $B_{\rm p} = 10^{12}$ G, we get maximum $\beta \sim 293$, which is close to Litwin's threshold for the same mound $\beta_{\rm T} \sim 260$. For higher mounds, $\beta_{\rm T}$ decreases with increase in $Z_{\rm c}$ and is much smaller than the maximum β obtained from our GS solutions. For example, for a filled mound with $Z_{\rm c} = 65$ m and $B_{\rm p} = 10^{12}$ G, $\beta_{\rm T} \sim 180$ whereas maximum $\beta \sim 911$ from the GS solution (see Fig 14). Hence, results from 2D simulations cannot rule out the presence of such modes in a 3D setup. Also, interchange mode instabilities (Chen 1984) can be excited in 3D simulation runs, as is seen in other examples of confined plasmas, e.g. in tokamak reactors. Work on 3D stability analysis of accretion mounds is currently underway and will be addressed in a forthcoming publication (Mukherjee, Bhattacharya and Mignone, in preparation).

(ii) **Instabilities due to excess mass:** from our 2D simulations we have found that the addition of excess mass destabilizes the equilibrium due to gravity-driven magnetic Rayleigh–Taylor type instabilities. For mounds with higher mass, the GS solutions have large radial (horizontal) component of magnetic field, which being perpendicular to gravity are also prone to Parker type instabilities (Cumming et al. 2001; Melatos & Phinney 2001). Topologically disconnected closed loops are formed beyond a threshold perturbation strength $\eta_{\rm T}$.

From the expression of the energy integral for linear perturbations (Litwin et al. 2001) on an adiabatic plasma ($p = k\rho^{\gamma}$), we have

$$\delta W = \frac{1}{2}\int {\rm d}^3x \Bigg\{ \frac{\tilde{B}_{\perp}^2}{4\pi} + \frac{B^2}{4\pi}\left(\nabla\cdot\boldsymbol{\xi}_{\perp} + 2\boldsymbol{\kappa}_{\rm c}\cdot\boldsymbol{\xi}_{\perp}\right)^2 + \gamma p\left(\nabla\cdot\boldsymbol{\xi} - 2\boldsymbol{\kappa}_g\cdot\boldsymbol{\xi}\right)^2 - 2(\boldsymbol{\kappa}_c + \nabla\phi/(2c_{\rm s}^2))\cdot\boldsymbol{\xi}_{\perp}(\nabla p + \rho\nabla\phi)\cdot\boldsymbol{\xi}_{\perp} \Bigg\}, \quad (15)$$

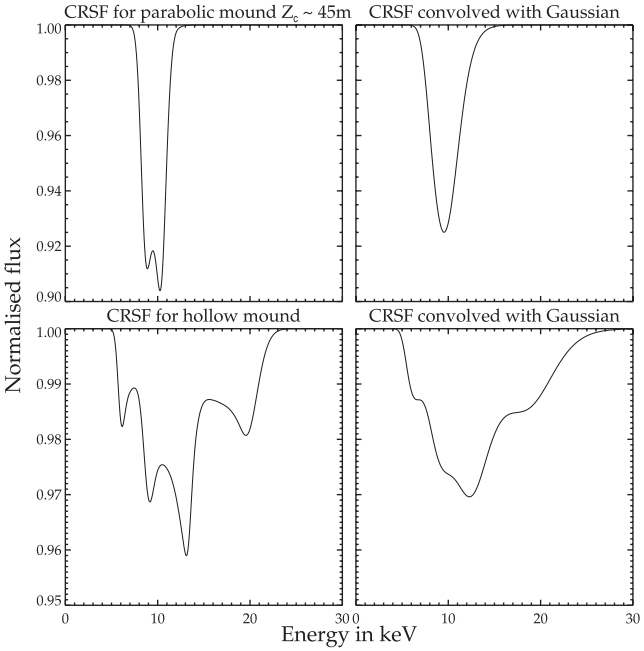

Figure 12. Top: CRSF from a filled mound of central height $Z_c \sim 45$ m and $B_p \sim 10^{12}$ G. The right-hand panel gives the spectra convolved with a Gaussian (standard deviation 10 per cent of local energy) to simulate finite detector resolution. Bottom: CRSF from a hollow mound with $Z_c = 45$ m and $B_p = 10^{12}$ G, with the right-hand panel giving the convolved spectra as before. The CRSF from hollow mounds show a much broader spectra due to contribution from different parts of the mound with large variations in the magnetic field.

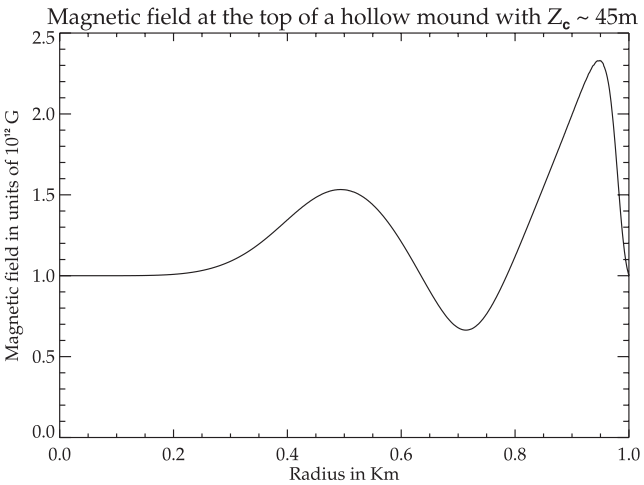

Figure 13. The magnetic field at the top of the hollow mound in Fig. 9. Field lines are pushed on either side of the apex ($r \sim 698$ m) of the mound resulting in decrease in field at the apex and increase in field strength on either side. Starting from a polar magnetic field strength $B_p = 10^{12}$ G, from our GS solution we get minimum field at the top $\sim 6.63 \times 10^{11}$ G and maximum field of $\sim 2.33 \times 10^{12}$ G.

where ξ is the plasma displacement, $\tilde{\boldsymbol{B}} = \nabla \times (\boldsymbol{\xi} \times \boldsymbol{B})$ is the perturbed magnetic field, $\boldsymbol{\kappa}_c = (\boldsymbol{b} \cdot \nabla)\boldsymbol{b}$ is the magnetic field curvature vector, c_s is the sound speed and ϕ the gravitational potential. B_ϕ is zero for our case.

Instabilities will develop if the negative contribution from any (or all) of the terms containing field curvature, pressure gradient

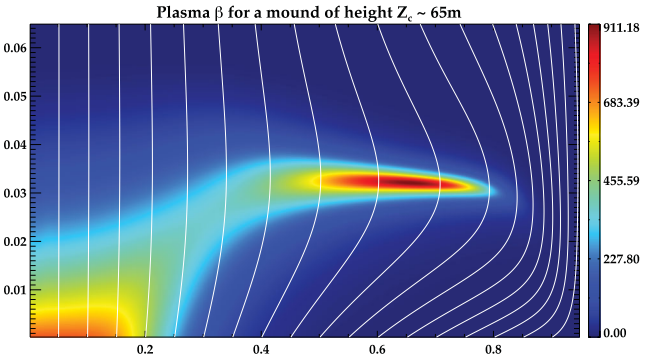

Figure 14. Plasma β (ratio of plasma pressure to magnetic pressure) for a GS solution of a mound of height $Z_c \sim 65$ m and $B_p \sim 10^{12}$ G. The vertical and horizontal axes are the height and radius, respectively, expressed in kilometres. The maximum plasma β ($\sim$911) occurs along the central red horizontal patch near the regions of maximum curvature of the magnetic field lines (represented in white). At the regions of high β, the plasma is primarily supported by tension from curvature of field lines. Such regions are prone to pressure-driven instabilities, and show formation of closed loops when perturbed.

and gravity overcomes the stabilizing effects of the magnetic and pressure compression terms.[4] Hence, it is not a surprise that the closed loops are formed in regions with the largest curvature in field lines. This also corresponds to the regions with high plasma β, e.g. the red region in the middle of Fig. 14 where $\beta \sim 911$. Pressure-driven instabilities typically lead to a threshold plasma β beyond which instabilities are triggered (e.g. Freidberg 1982; Litwin et al. 2001). For mounds near the stability threshold, e.g. $Z_c \sim 72$ m at $B_p = 10^{12}$ G, the maximum plasma β is as high as $\sim 1.26 \times 10^4$.

The magnitude of η_T decreases with increase in mound height, with $\eta_T \to 0$ as $Z_c \to Z_{max}$, indicating inherent unstable nature of the mound for the modes under investigation. This corroborates the result of MB12 that GS solutions do not converge beyond a threshold height. The tests involving addition of mass are not meant to reflect realistic accretion rates. Although the amount of excess mass added in our simulations is small ($\sim 7.6 \times 10^{-15}\,M_\odot$ for $\eta = 5$ per cent perturbation on 65 m mound), in a real system such mass will be accumulated slowly as mounds of larger mass are built. Effects of such inflow of material on an initially static mound have not been addressed here. However, from our current 2D simulations we conclude that for large mound masses, gravity- and pressure-driven modes result in the onset of MHD instabilities and no static equilibrium solution can be found beyond a threshold Z_{max}.

Buoyancy related instabilities due to the formation of topologically disconnected closed loops have previously been reported in the static mound simulations of Hameury et al. (1983) and Payne & Melatos (2004) and also dynamic MHD simulations by Vigelius & Melatos (2008, hereafter VM08). However, the threshold mass of the mound for the formation of closed loops in PM04 and VM08 is $M \sim 10^{-5}\,M_\odot$, which is much larger than the mass of the mounds in this work. This may be due to the following differences in approach.

(a) PM04 and VM08 in their treatment consider spherical polar geometry and populate all field lines up to the equator, whereas we confine the accretion mounds strictly within the polar cap radius.

[4] Necessary and sufficient condition for instability is $\delta w < 0$ (Bernstein et al. 1958).

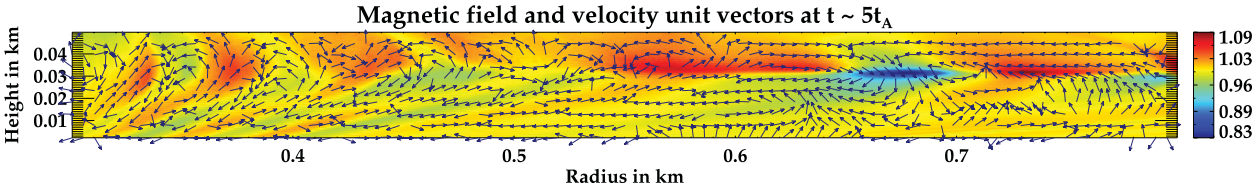

Figure 15. Ratio of the magnetic field to its local equilibrium value for a barotropic simulation with random velocity perturbation of strength $\eta = 15$ per cent of local sound speed (maximum initial velocity ∼0.35, in normalized units). The velocity unit vectors are plotted to show the nature of the flow. The bunching of magnetic field takes place in the radial direction as local eddies are formed. The system settles down to a steady state with flow velocities less than $\sim 7.54 \times 10^{-3}$ (in normalized units) at $t \sim 5t_{\rm A}$.

Populating all field lines up to the equator provides lateral pressure support to the polar mound which can then hold a larger mass.

(b) Plasma pressure due to isothermal EOS by PM04 and VM08 is several orders of magnitude less than the degenerate *Fermi* pressure used in our treatment, which results in higher plasma β in our simulation. Such a system is more prone to pressure-driven MHD instabilities, e.g. Freidberg (1982).

(iii) **Adiabatic versus barotropic:** we have also performed barotropic simulations with PLUTO for which the energy equation becomes redundant as pressure is evaluated from $p = k\rho^{\gamma}$, with k a constant. This is similar to the isothermal setup of MHD simulations. Results from adiabatic and barotropic modes are similar when perturbations are applied to velocity and magnetic fields. See Fig. 15 for the results of velocity perturbation with barotropic simulation ($\eta = 15$ per cent of local sound speed). The magnetic field bunches in the radial direction and local eddies are set up. The system settles down to a steady state with flow velocities reduced by more than three orders of magnitude at $t \sim 5t_{\rm A}$. Similar results are also obtained for adiabatic EOS.

However, density perturbations behave differently in barotropic and adiabatic simulations. For a barotropic simulation, positive density perturbations on an initial static equilibrium create regions of excess pressure. The perturbed regions with high local pressure overcome the downward gravitational force and are quickly transported vertically upwards. Hence, to study the effect of gravity-driven modes due to the descent of added matter, adiabatic simulations have been performed in this work.

(iv) **Hollow mounds – structure and stability:** we have solved the GS equation for mounds with hollow interiors. The hollow mounds show considerable distortion of the magnetic field on both sides of the maximum height to support the confined matter. There is a decrease in field near the ridge apex as field lines are pushed to either side. Closed loops form when excess mass is added to the equilibrium solution. The closed loops migrate to either side and eventually dissipate.

The fixed gradient boundary condition can induce artificial stability as it results in line tying type boundaries, which are known to give extra stability. In a real system, the plasmoids will be eventually ejected from the system. Plasma travelling inwards on closed loops may then eventually fill up the hollow. However, there was no significant mass-loss seen in our 2D simulations.

(v) **Hollow mounds – CRSF:** CRSF from hollow mounds have been explored. From the simulation of the spectra integrated over the entire mound we see the following.

(a) Cyclotron emission from the top of hollow mounds show complex fundamental features in the line shape (harmonics have not been evaluated), due to the large variations in magnetic field on the top of such mounds. This is similar to what is observed in the spectra of V0332+53 (Mowlavi et al. 2006; Nakajima, Mihara & Makishima 2010) which is conjectured to have a hollow column geometry (Ferrigno et al. 2011). Complex line shapes have also been predicted previously for strong non-dipolar local magnetic field by Nishimura (2008, 2011).

(b) Convolving the CRSF with a Gaussian to account for finite energy resolution of detectors, we see that the resultant CRSF has the structure of a broad absorption envelope.

Thus, CRSF from hollow mounds will be characterized by broad line widths and complex structures in the line shape, which may be observed with improved detector resolution.

Thus, we conclude from this work that accretion mounds on neutron stars in HMXB are stable up to a threshold height and mass, beyond which MHD instabilities will disrupt the equilibria. Structure and stability of hollow mounds have been explored. It is shown that CRSF from such mounds will be characterized by broad features with a complex line shape. More work needs to be done to explore the 3D stability of such systems and the effect of non-axisymmetric modes on the field structure and cyclotron emission from such mounds.

ACKNOWLEDGEMENTS

We thank CSIR India for Junior Research Fellow Grant, award no 09/545(0034)/2009-EMR-I. We also thank Dr Petros Tzeferacos for his help and suggestions in setting up the boundary conditions in the PLUTO simulations. We thank Dr Kandaswamy Subramanian, Dr Ranjeev Misra and Sandeep Kumar from IUCAA for useful discussions and suggestions during the work, and IUCAA HPC team for their help in using the IUCAA HPC where most of the numerical computations were carried out. We also thank the anonymous referee for the detailed comments which have greatly helped in improving the work. DB acknowledges the hospitality of ISSI, Berne and discussions with the Magnet collaboration which have benefited the paper.

REFERENCES

Araya R. A., Harding A. K., 1999, ApJ, 517, 334
Araya-Góchez R. A., Harding A. K., 2000, ApJ, 544, 1067
Basko M. M., Sunyaev R. A., 1976, MNRAS, 175, 395
Becker P. A., Wolff M. T., 2007, ApJ, 654, 435
Becker P. A. et al., 2012, A&A, 544, A123
Beloborodov A. M., 2002, ApJ, 566, L85
Bernstein I. B., Frieman E. A., Kruskal M. D., Kulsrud R. M., 1958, R. Soc. Lond. Proc. Ser. A, 244, 17
Bhattacharya D., van den Heuvel E. P. J., 1991, Phys. Rep., 203, 1
Brown E. F., Bildsten L., 1998, ApJ, 496, 915
Caballero I., Kraus U., Santangelo A., Sasaki M., Kretschmar P., 2011, A&A, 526, A131

Chen F. F., 1984, Introduction to Plasma Physics and Controlled Fusion. Springer, Berlin
Choudhuri A. R., Konar S., 2002, MNRAS, 332, 933
Coburn W., Heindl W. A., Rothschild R. E., Gruber D. E., Kreykenbohm I., Wilms J., Kretschmar P., Staubert R., 2002, ApJ, 580, 394
Colella P., Woodward P. R., 1984, J. Comput. Phys., 54, 174
Cumming A., Zweibel E., Bildsten L., 2001, ApJ, 557, 958
Davidson K., Ostriker J. P., 1973, ApJ, 179, 585
Dedner A., Kemm F., Kröner D., Munz C.-D., Schnitzer T., Wesenberg M., 2002, JJ. Comput. Phys., 175, 645
Ferrigno C., Falanga M., Bozzo E., Becker P. A., Klochkov D., Santangelo A., 2011, A&A, 532, A76
Freidberg J. P., 1982, Rev. Mod. Phys., 54, 801
Fürst F., Kreykenbohm I., Suchy S., Barragán L., Wilms J., Rothschild R. E., Pottschmidt K., 2011, A&A, 525, A73
Ghosh P., Lamb F. K., 1978, ApJ, 223, L83
Ghosh P., Lamb F. K., 1979, ApJ, 232, 259
Ghosh P., Pethick C. J., Lamb F. K., 1977, ApJ, 217, 578
Hameury J. M., Bonazzola S., Heyvaerts J., Lasota J. P., 1983, A&A, 128, 369
Harding A. K., Preece R., 1987, ApJ, 319, 939
Heindl W. A., Rothschild R. E., Coburn W., Staubert R., Wilms J., Kreykenbohm I., Kretschmar P., 2004, in Kaaret P., Lamb F. K., Swank J. H., eds, AIP Conf. Ser. Vol. 714, Timing and Spectroscopy of Accreting X-ray Pulsars: the State of Cyclotron Line Studies. Am. Inst. Phys., New York, p. 323
Kajava J. J. E., Ibragimov A., Annala M., Patruno A., Poutanen J., 2011, MNRAS, 417, 1454
Klochkov D. et al., 2008, A&A, 482, 907
Koldoba A. V., Lovelace R. V. E., Ustyugova G. V., Romanova M. M., 2002, ApJ, 123, 2019
Konar S., Choudhuri A. R., 2004, MNRAS, 348, 661
Kraus U., 2001, ApJ, 563, 289
Kraus U., Nollert H.-P., Ruder H., Riffert H., 1995, ApJ, 450, 763
Leahy D. A., 1991, MNRAS, 251, 203
Litwin C., Brown E. F., Rosner R., 2001, ApJ, 553, 788
Lutovinov A., Tsygankov S., 2008, in Axelsson M., ed., AIP Conf. Ser., Vol. 1054, X-ray Pulsars through the Eyes of INTEGRAL. Am. Inst. Phys., New York, p. 191
Melatos A., Phinney E. S., 2001, Publ. Astron. Soc. Aust., 18, 421
Mignone A., Tzeferacos P., 2010, J. Comput. Phys., 229, 2117
Mignone A., Bodo G., Massaglia S., Matsakos T., Tesileanu O., Zanni C., Ferrari A., 2007, ApJS, 170, 228
Mignone A., Tzeferacos P., Bodo G., 2010, J. Comput. Phys., 229, 5896
Mihara T. et al., 2007, Prog. Theor. Phys. Suppl., 169, 191
Miyoshi T., Kusano K., 2005, J. Comput. Phys., 208, 315
Mowlavi N. et al., 2006, A&A, 451, 187
Mukherjee D., Bhattacharya D., 2012, MNRAS, 420, 720
Nakajima M., Mihara T., Makishima K., 2010, ApJ, 710, 1755
Nishimura O., 2008, ApJ, 672, 1127
Nishimura O., 2011, ApJ, 730, 106
Panchenko I. E., Postnov K. A., 1994, A&A, 286, 497
Payne D. J. B., Melatos A., 2004, MNRAS, 351, 569
Payne D. J. B., Melatos A., 2007, MNRAS, 376, 609
Poutanen J., Beloborodov A. M., 2006, MNRAS, 373, 836
Poutanen J., Ibragimov A., Annala M., 2009, ApJ, 706, L129
Press W. H., Teukolsky S. A., Vetterling W. T., Flannery B. P., 1993, Numerical Recipes in C. Cambridge Univ. Press, Cambridge
Riffert H., Nollert H.-P., Kraus U., Ruder H., 1993, ApJ, 406, 185
Romani R. W., 1990, Nat, 347, 741
Romanova M. M., Ustyugova G. V., Koldoba A. V., Wick J. V., Lovelace R. V. E., 2003, ApJ, 595, 1009
Schönherr G., Wilms J., Kretschmar P., Kreykenbohm I., Santangelo A., Rothschild R. E., Coburn W., Staubert R., 2007, A&A, 472, 353
Shakura N. I., Postnov K. A., Prokhorov M. E., 1991, Sov. Astron. Lett., 17, 339
Toro E. F., 2008, Riemann Solver and Numerical Methods for Fluid Dynamics. Springer, Berlin
Vigelius M., Melatos A., 2008, MNRAS, 386, 1294
Vigelius M., Melatos A., 2009, MNRAS, 395, 1985

APPENDIX A: SHIELDING OF RADIATION FROM INNER WALLS OF HOLLOW MOUNDS

In HMXBs an accretion column is formed by the infalling matter after it passes through a shock which may be several kilometres from the surface of the star, depending on the accretion rate (e.g. Basko & Sunyaev 1976; Becker & Wolff 2007; Becker et al. 2012). In this work, we consider the spectra generated from the mound without incorporating the effects of scattering from the overlying accretion column. This is valid for systems with low accretion rates and optically thin columns. The emission from the mound will then be directly visible and effects of overlying column will be small. However for systems with optically thick columns and large accretion rates, the emission from the mound will be obscured by scattering and absorption in the column. A proper Monte Carlo simulation of the radiative transfer through the column must be carried out to address such cases, which will be reported in a future work (Kumar, Bhattacharya and Mukherjee, in preparation).

The rays of light coming from the hollow region can be blocked by the inner walls of the mound on the opposite side. Such rays will not contribute to the total spectra. The path of the emitted ray lies in the plane defined by the radius vector from the origin (centre of the neutron star) to the point of emission ($\boldsymbol{r}$) and the unit vector along the los $\hat{\boldsymbol{n}}_\psi$ (see e.g. Beloborodov 2002; Poutanen & Beloborodov 2006; Mukherjee & Bhattacharya 2012). To exclude rays that may be blocked by the inner walls of the hollow mound, we first find the point where the plane defined by $\boldsymbol{r}$ and $\hat{\boldsymbol{n}}_\psi$ passes through the top of the mound $\boldsymbol{r}_c$ as in Fig. A1. The radial and vertical coordinates of $\boldsymbol{r}_c$ (r_c and z_c, respectively) are found by fitting a polynomial to the top of the mound obtained from the GS solution and evaluating the coordinate where z is maximum. Since the three vectors $\boldsymbol{r}$, $\hat{\boldsymbol{n}}_\psi$ and $\boldsymbol{r}_c$ lie in the same plane, the angular coordinate ϕ_c of $\boldsymbol{r}_c$ is found from the condition

$$\boldsymbol{r}_c \cdot \left(\boldsymbol{r} \times \hat{\boldsymbol{n}}_\psi\right) = \boldsymbol{0}. \tag{A1}$$

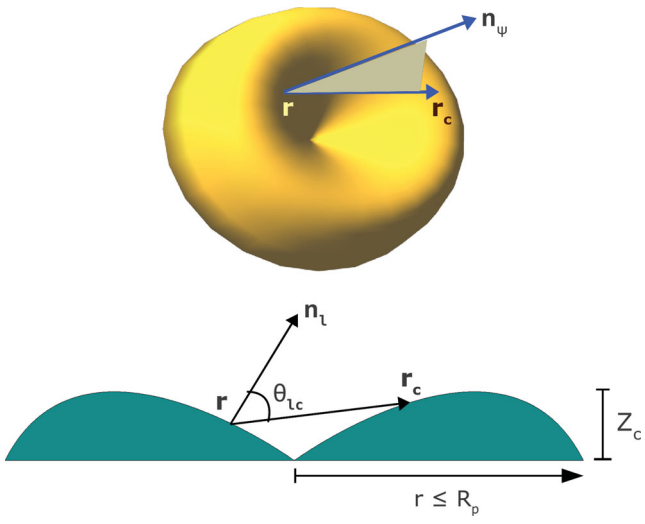

Figure A1. Top: a 3D schematic representation of the hollow mound. The vectors $\boldsymbol{n}_\psi$ and $\boldsymbol{r}_c - \boldsymbol{r}$ denote the plane where the path of the emitted ray to the observer lie. Bottom: a cross-section of the mound along the plane of the emitted ray to the observer and the location where the plane cuts the mound on the opposite side.

Following MB12, we use the following definitions for the vectors $\hat{\boldsymbol{n}}_\psi \equiv (n_{\psi x}, n_{\psi y}, n_{\psi z}) \equiv (\sin i \sin\omega, \sin i \cos\omega, \cos i)$ and $\boldsymbol{r} \equiv (x, y, z) \equiv \{\rho\cos\phi, \rho\cos\eta_{\rm p}\sin\phi + (\xi + R_{\rm s})\sin\eta_{\rm p}, (\xi + R_s)\cos\eta_{\rm p} - \rho\sin\eta_{\rm p}\sin\phi\}$, where i is the azimuthal angle of the observer's los with respect to the spin axis, ω is the spin-phase angle, (ρ, ϕ, ξ) are coordinates of the emitting region in the polar cap frame with cylindrical coordinate system, $R_{\rm s}$ is the neutron star radius and $\eta_{\rm p}$ is the azimuthal angle of the centre of the polar cap. Using the above, we can rewrite equation (A1) as

$$A_{\rm c}\cos\phi_{\rm c} + B_{\rm c}\sin\phi_{\rm c} + C_{\rm c} = 0, \tag{A2}$$

where

$$A_{\rm c} = \rho_{\rm c}(yn_{\psi z} - zn_{\psi y})$$

$$B_{\rm c} = \rho_{\rm c}\cos\eta_{\rm p}(zn_{\psi x} - xn_{\psi z}) - \rho_{\rm c}\sin\eta_{\rm p}(xn_{\psi y} - yn_{\psi x})$$

$$C_{\rm c} = (\xi_{\rm c} + R_{\rm s})\{\sin\eta_{\rm p}(zn_{\psi x} - xn_{\psi z}) + \cos\eta_{\rm p}(xn_{\psi y} - yn_{\psi x})\}.$$

Equation (A2) is solved using a modified Newton–Raphson scheme following Press et al. (1993). After finding the coordinate of $\boldsymbol{r}_{\rm c}$, we evaluate the angle $\theta_{\rm lc}$ (see Fig. A1) between the local normal ($\hat{\boldsymbol{n}}_l$) and the radius vector from the point of emission to the top of the mound on the other side

$$\cos\theta_{\rm lc} = \hat{\boldsymbol{n}}_{\rm l}\cdot\frac{(\boldsymbol{r}_{\rm c} - \boldsymbol{r})}{|\boldsymbol{r}_{\rm c} - \boldsymbol{r}|}. \tag{A3}$$

The normal vector is found as outlined in MB12 by evaluating the slope $m_{\rm s} = {\rm d}\xi_{\rm top}/{\rm d}\rho$ of the function $\xi_{\rm top} = f(\rho)$ (ρ being the radial coordinate) that fits the top profile of the mound obtained from the GS solutions: $\hat{\boldsymbol{n}}_{\rm l} \equiv \{-\sin\theta_{\rm s}\cos\phi, -\sin\theta_{\rm s}\cos\eta_{\rm p}\sin\phi + \cos\theta_{\rm s}\sin\eta_{\rm p}, \cos\theta_{\rm s}\cos\eta_{\rm p} + \sin\theta_{\rm s}\sin\eta_{\rm p}\sin\phi\}$, where $\sin\theta_{\rm s} = \frac{m_{\rm s}}{\sqrt{1+m_{\rm s}^2}}$ and $\cos\theta_{\rm s} = \frac{1}{\sqrt{1+m_{\rm s}^2}}$. Using the above definitions of the vectors, one can write

$$\hat{\boldsymbol{n}}_{\rm l}\cdot(\boldsymbol{r}_{\rm c} - \boldsymbol{r}) = \cos\theta_{\rm s}(\xi_{\rm c} - \xi) + \sin\theta_{\rm s}(\rho\cos\phi - \rho_{\rm c}\cos\phi_{\rm c}) \times(\sin\phi + \cos\phi)$$

$$|\boldsymbol{r}_{\rm c} - \boldsymbol{r}|^2 = \rho^2 + \rho_{\rm c}^2 + (\xi - \xi_{\rm c})^2 - 2\rho\rho_{\rm c}(\cos\phi\cos\phi_{\rm c} + \sin\phi\sin\phi_{\rm c}).$$

Any ray with emission angle larger than $\theta_{\rm lc}$ will not contribute to the total spectra. This implicitly assumes that light will travel in a straight line and curvature effects from bending due to gravity are ignored for such short paths.

More accurate methods should be used to calculate the tangent vector from the point of emission to the mound surface on the other side. However, this involves more computation, and for sharp profiles of the hollow mound used approximating the tangent point as the top of the mound will result in only a small correction.

This paper has been typeset from a TEX/LATEX file prepared by the author.